Research Paper

Journal of Engineering and Technological Sciences

Damage Tolerance Characteristics of Woven-Carbon/Epoxy Laminates under Low-Velocity Impact: Insights from Tests and Simulations

Muhammad Giri Suada[1,*], Haroen Romadon[2] & Hendri Syamsudin[1]

[1]Faculty of Mechanical and Aerospace Engineering, Institut Teknologi Bandung, Jalan Ganesa No. 10, Bandung, 40132, Indonesia
[2]Indonesian Aircraft Industry, Jalan Pajajaran No. 154, Bandung, 40174, Indonesia

*Corresponding author: mgsuada@gmail.com

Abstract

This study investigated the low-velocity impact damage tolerance of woven AS4/8552 carbon/epoxy laminates through combined drop-weight testing and finite element simulation. Five eight-layer [|±45°|/|90°/0°|/|±45°|/|0°/90°|]s specimens were impacted at 8.25 J, and the resulting internal damage was characterized using ultrasonic C-scanning. A detailed FEM model was developed in ABAQUS using SC8R continuum-shell elements for the laminae and COH3D8 cohesive-zone elements for interlaminar delamination, with Hashin failure criteria and the Benzeggagh–Kenane mixed-mode fracture law governing damage initiation and propagation. The numerical model reproduced the main experimental impact response, predicting a peak force of 4950 N compared with the experimental mean of 4360 N, corresponding to a 13% overestimation. The predicted delamination footprint also agreed well with C-scan observations, which showed delamination diameters ranging from 15.9 to 19.9 mm, with an average of 17.9 mm. However, the simulation underestimated absorbed energy by approximately 40% and produced smoother delamination boundaries than those observed experimentally. These discrepancies are attributed to the homogeneous cohesive-zone representation and continuum-shell formulation, which cannot fully capture fiber bridging, microcracking, interlaminar friction, and local stress perturbations caused by woven yarn undulations. The results demonstrate that the proposed framework is effective for predicting the global delamination extent and impact response of aerospace-representative woven laminates, while highlighting key improvements required for higher-fidelity damage-tolerance assessment.

Keywords: *barely visible impact damage; composite; delamination; finite element method; low-velocity impact; woven-ply.*

Introduction

The resistance of composite laminates to low-velocity impact has become a prominent research area, particularly for unidirectional (UD) ply laminates, as exemplified in prior studies by Anuse et al. (2022), Fan et al. (2022), Tao et al. (2021), and Shi et al. (2020). Such impact often leads to barely visible impact damage (BVID), which can evolve into serious problems such as delamination. Tao et al. (2021) determined how ply clustering affects the extent of impact-induced damage, emphasizing its role in diminishing structural stiffness and compressive strength. Their in-depth analysis assessed UD prepreg materials with various stacking sequences, ultimately revealing that low-velocity impact loading predominantly caused delamination.

Owing to their industrial importance, researchers have focused on the resilience of woven-ply composite laminates under low-velocity impact conditions. Fanteria et al. (2017) explored the correlation between low-velocity impact damage and the residual compressive strength, particularly for woven-ply laminates. Grasso et al. (2019) evaluated the impact characteristics of woven-ply laminate plates, whereas Castellanos et al. (2019) studied the behavior of woven-ply carbon composites under low-velocity impact in extremely cold environments. Ma et al. (2024) comparatively studied the impact resistance of UD, woven-ply, and hybrid composite laminates, revealing that similar to UD laminates, woven-ply laminates also experienced delamination, significantly reducing their compressive strength. Taken together, these studies underscored the importance of accurately predicting delamination when modeling the damage and subsequent loss of compressive strength in composite laminates after low-velocity impact.

ISSN: 2337-5779
J. Eng. Technol. Sci. Vol. 58, No. 4, 2026, 602-612
DOI: 10.5614/j.eng.technol.sci.2026.58.4.10

DOI: 10.5614/j.eng.technol.sci.2026.58.4.10

Furthermore, recent studies have extensively investigated the impact damage mechanisms and residual strength of composite repairs and hybrid structures. For instance, Liu et al. (2019) examined the impact damage and residual load capacity of composite stepped bonding repairs, revealing critical energy thresholds for adhesive failure. Similarly, Liu et al. (2017) analyzed the tension-after-impact capacity in scarf-repaired primary load-bearing structures and identified adhesive damage as a key factor influencing the residual strength. For ceramic-matrix composites, Liu et al. (2024) proposed a 3D FE-PDM approach to predict low-velocity impact damage in laminated C/SiC structures, demonstrating the importance of strain-controlled damage criteria. Furthermore, hybrid composite systems for aerospace applications have been studied for their impact and compression-after-impact (CAI) performance, highlighting the need for multi-material damage modeling strategies. For example, Liu et al. (2026) analyzed the impact damage and compression of CFRP–GFRP hybrid composite materials applied as smart-skins for aerospace applications.

Although low-velocity impact on composite laminates has been extensively investigated, most prior studies focused on UD ply systems. Woven-ply architectures, which are increasingly being adopted in aerospace secondary structures for their balanced in-plane properties, exhibit distinct damage mechanisms that are not fully captured by UD-calibrated models, such as fiber-undulation-induced stress concentrations and shear-driven irregular delamination. Furthermore, predicting BVID and the delamination morphology remains a critical challenge for damage-tolerance certification, particularly for layups with significant orientation mismatches (e.g., ±45°/0° interfaces). This study addresses these gaps by: (1) experimentally characterizing the impact damage in woven AS4/8552 laminates with an aerospace-representative stacking sequence, (2) developing a cohesive-zone finite element method (FEM) framework validated against C-scan delamination profiles, and (3) explicitly quantifying model limitations related to fiber bridging and microcracking. The results of these analyses provide actionable insights for improving numerical damage prediction in woven composite structures.

Simulations were conducted using ABAQUS FEM software, and the accuracy of the model was validated against experimental results, including the delamination magnitude, energy absorption, force–displacement behavior, and dynamic responses. The primary objective was to precisely predict the delamination, the energy dissipated during impact, and dynamic behaviors. Notably, the proposed numerical method aligned with that of similar experimental and numerical investigations conducted by the authors on UD carbon/epoxy laminates (Suada et al. 2022), which demonstrated strong agreement between the simulated and experimental delamination patterns.

Experimental Methods

The test specimen comprised eight layers of Hexply AS4/8552 arranged in the stacking sequence of [|±45°|/|90°/0°|/|±45°|/|0°/90°|]s. Five specimens were manufactured and evaluated utilizing an impact energy of 8.25 J, which was controlled to ensure that the resulting damage met the BVID criteria outlined by Fawcett et al. (2006). The average specimen thickness was 3.06 mm. An INSTRON 9350 drop-weight testing machine was used, and the testing standard ASTM D7136/D7136M-25 (2025) was adopted.

The stacking sequence $[|\pm45°|/|90°/0°|/|\pm45°|/|0°/90°|]_s$ was selected in accordance with industrial design standards for secondary aerospace structures, as advised by our industry partner, Indonesian Aircraft Industry. This configuration represents a common design for components subjected to multi-axial loading, as it balances in-plane stiffness (via |0°/90°| plies) with shear resistance and damage tolerance (via |±45°| plies). Academically, this sequence is particularly meaningful for woven composites because the interfaces between the |±45°| and |0°/90°| plies create significant mismatches in the stiffness coefficients and Poisson's ratios. These mismatches generate complex interlaminar stress states that drive delamination initiation differently from that in UD systems, making this layup a critical case study for advancing the prediction of damage tolerance in woven architectures.

Numerical Simulations and Material Data

This study explored the influence of mesh element sizing on the accuracy and computational efficiency of the simulation outcomes. In particular, the simulation precision was balanced with the duration of the computational processes. As depicted in Figure 1, the mesh utilized in this study represented the lamina as a single-layer configuration subdivided into SC8R elements. To model the interface between the lamina, COH3D8 cohesive zone elements were incorporated. The SC8R element is an eight-node, solid-like continuum shell element with reduced integration, as described by Dassault Systèmes (2024). The element dimensions were determined according to the guidelines of Tosti Balducci and Chen (2024), which emphasized that cohesive elements must be sufficiently small to accurately capture the steep stress gradients near the delamination. Based on the authors' experience (Suada et al. 2022), the SC8R element dimensions adopted in this study were set to 1.25, 1.25, and 0.23 mm in length, width, and thickness, respectively.

Similarly, the COH3D8 elements were assigned a length, width, and thickness of 1.25, 1.25, and 0.006 mm, respectively. These smallest cohesive elements were strategically placed in regions susceptible to localized damage, whereas a coarser mesh was applied in noncritical areas to optimize computational resources. The fixture was modeled as being in contact with the lamina, and compressive forces were not applied. Constraints were imposed to restrict the translational and rotational degrees of freedom in all directions. The impactor a rigid spherical body calibrated to deliver an impact energy of 8.25 J. The contact definitions were thoroughly evaluated in this study. Translational movement was allowed exclusively along the transverse axis, and all other degrees of freedom were fixed. Gravitational effects are incorporated to enhance the accuracy of the numerical analyses. A general contact algorithm was employed to model the interactions between the laminates, impactors, and fixtures. This meticulous approach to defining the contact conditions ensured the fidelity and reliability of the simulation results.

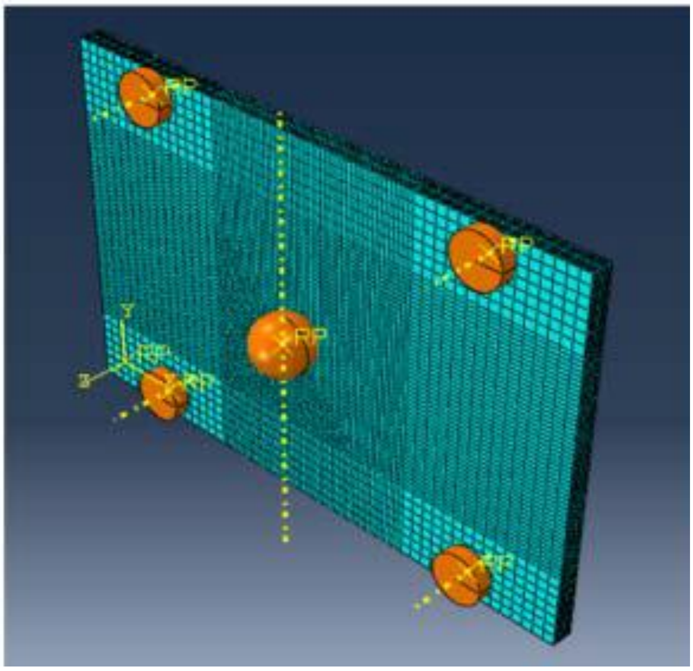

Figure 1 FEM model of the eight-layer configuration [|±45°|/|90°/0°|/|±45°|/|0°/90°|]s for the woven carbon composite panel.

The friction coefficient (μ) was established at 0.6. The material properties of the AS4/8552 woven carbon/epoxy are listed in Tables 1 and 2.

Table 1 Layer material properties

Properties	Values
Longitudinal stiffness, E_{11} (GPa)	70
Transverse stiffness, E_{22} (GPa)	65
Shear modulus, G_{12} (GPa)	5.5
Poisson's ratio, μ_{12}	0.048
Density (ton/mm^3)	16×10^{-8}
Tensional longitudinal strength, X_T (MPa)	800.
Compressional longitudinal strength, X_C (MPa)	700.
Tensional transverse strength, Y_T (MPa)	750.
Compressional transverse strength, Y_C (MPa)	650.
Shear in-plane strength, S_{12} (MPa)	80.
Shear transverse strength, S_{23} (MPa)	5.5

The material properties for the AS4/8552 woven carbon/epoxy system (Tables 1 and 2) were adopted from the Hexcel Corporation product data sheet (Hexcel Corporation, 2020). The interlaminar fracture energies were adjusted slightly based on laboratory coupon tests to account for woven architecture effects, following recommendations by Ao et al. (2022).

DOI: 10.5614/j.eng.technol.sci.2026.58.4.10

Table 2 Interfacial properties

Properties	Values
Normal stiffness, k_n (MPa/mm)	37,000.
Shear stiffness, k_t and k_s (MPa/mm)	19,000.
Max normal stress, N_{max} (MPa)	90
Max shear stress, $S_{max} = T_{max}$ (MPa)	80
Normal fracture energy (kJ/m^2)	0.8
Shear fracture energy (kJ/m^2)	1.5
Density, ρ (ton/mm^3)	1.3×10^{-9}

Failure Models

Progressive damage processes can be categorized into layer- and interface-based damage models. The layer-damage model predicts damage initiation and progression within the lamina. This damage manifests as fiber failure under tension or compression, including longitudinal and transverse failure. For the layer damage model, the present numerical analysis used the failure model described by Hashin, (1980), which was originally developed for UD laminae. In this study, each woven ply was modeled as a homogeneous orthotropic equivalent layer, where the warp and weft directions corresponded to the longitudinal (1) and transverse (2) axes of the Hashin criteria, respectively. The material properties listed in Table 1 represent the effective homogenized properties of the woven architecture. This macromechanical approach follows the methodology established by Sanga et al. (2016) for woven composite structures, providing a computationally efficient prediction of global damage initiation while acknowledging that intra-ply yarn-level failures are averaged within the equivalent layer properties. The interface damage model focuses on predicting and propagating delamination. A concise overview of the damage progression model is as follows:

Layer Failure Model

The damage models used four criteria: longitudinal fiber tension, longitudinal fiber compression, transverse matrix tension, and transverse matrix compression. These criteria were as follows:

Longitudinal fiber tension $(\sigma_1 > 0)$

$$\mathrm{F}_{\mathrm{lt}}^2 = \left(\frac{\sigma_1}{\mathrm{X_T}}\right)^2 + \left(\frac{\sigma_{12}}{\mathrm{S}_{12}}\right)^2 \tag{1}$$

Longitudinal fiber compression $(\sigma_1 < 0)$

$$\mathrm{F}_{\mathrm{lc}}^2 = \left(\frac{\sigma_1}{\mathrm{X_C}}\right)^2 \tag{2}$$

Transversal matrix tension $(\sigma_2 > 0)$

$$\mathrm{F}_{\mathrm{Tt}}^2 = \left(\frac{\sigma_2}{\mathrm{Y_T}}\right)^2 + \left(\frac{\sigma_{12}}{\mathrm{S}_{12}}\right)^2 \tag{3}$$

Transversal matrix compression $(\sigma_2 < 0)$

$$\mathrm{F}_{\mathrm{Tc}}^2 = (\frac{\sigma_2}{2\mathrm{S}_{12}})^2 + \frac{\sigma_2}{\mathrm{Y_C}}\left[\left(\frac{\mathrm{Y_C}}{2\sigma_{12}}\right)^2 - 1\right] + \left(\frac{\sigma_{12}}{\mathrm{S}_{12}}\right) \tag{4}$$

Where X_t and X_C denote the tensile and compressive strengths along the longitudinal and fiber axes respectively, whereas Y_t and Y_C indicate the tensile and compressive strengths in the transverse and matrix directions, respectively. The values of these parameters are listed in Table 1. S12 shows the shear strength in the 1–2 plane. The components of the effective stress tensor, σ_1, σ_2, and σ_{12}, were evaluated through the following relation:

$$\sigma = \begin{bmatrix} \frac{1}{1-\mathrm{d_f}} & 0 & 0 \\ 0 & \frac{1}{1-\mathrm{d_m}} & 0 \\ 0 & 0 & \frac{1}{1-\mathrm{d_s}} \end{bmatrix} \hat{\sigma} \tag{5}$$

Where $\hat{\sigma}$ is the true stress tensor, and d_f, d_m, and d_s are internal damage variables that characterize longitudinal (fiber), transversal (matrix), and shear damage, respectively, which were defined by the corresponding damage variables d_f^t, d_f^c, d_m^t and d_m^c by

$$\mathrm{d_f} = \begin{cases} \mathrm{d_f^t} \text{ if } \sigma_1 \geq 0 \\ \mathrm{d_f^c} \text{ if } \sigma_1 < 0 \end{cases} \tag{6}$$

$$\mathrm{d_m} = \begin{cases} \mathrm{d_m^t} \text{ if } \sigma_2 \geq 0 \\ \mathrm{d_m^c} \text{ if } \sigma_2 < 0 \end{cases} \tag{7}$$

$$\mathrm{d_s} = 1 - (1 - \mathrm{d_f^t})(1 - \mathrm{d_f^c})(1 - \mathrm{d_m^t})(1 - \mathrm{d_m^c}) \tag{8}$$

Before the damage initiated and evolved inside the material, the initial conditions associated with the problem were $d_f^t = d_f^c = d_m^t = d_m^c = 0$.

Interface Failure Model

The practical applications of our method for modeling the of evolution of interlayer damage, which incorporates cohesive zone characteristics, are clearly significant. This interface component is essential for governing the interactions between two connected surfaces. The adhesion or separation is measured based on the displacement of the two surfaces. Relative displacement can occur in either the normal or shear direction, that is, the tractions (t_n, t_s, t_t) indicate the adhesive bonding of the two surfaces. The symbol tn represents traction in normal mode, while ts and tt are in two orthogonal shear directions, which are characterized as follows:

$$\{t\} = [K]\{\varepsilon\} \tag{9}$$

Vector $\{\varepsilon\}$ contains δ_n, δ_s, and δ_t, which are the relative displacements in the normal direction and two orthogonal relative displacements in the shear directions. The stiffness of the cohesive material is represented by a diagonal matrix [K] containing a normal stiffness k_n and two orthogonal shear stiffnesses k_s and k_t. Further, {t} represents the traction in three directions. Damage was initiated when the quadratic equation below exceeded 1.

$$\left(\frac{<t_n>}{N_{max}}\right)^2 + \left(\frac{t_s}{S_{max}}\right)^2 + \left(\frac{t_t}{T_{max}}\right)^2 = 1 \tag{10}$$

Note that $< t_n >$ represents the Macaulay bracket where, in this application, $< t_n > = \frac{1}{2}(|t_n| + t_n)$. The Macaulay brackets signify that a pure compressive deformation or stress state does not initiate damage. When the initial failure conditions are met, the stiffness undergoes linear softening, represented by the scalar variable d. The variable d ranges from 0 to 1, with 1 indicating material failure, in which case the material stiffness k is set to zero. Figure 2 illustrates the traction separation with softening behavior. The critical fracture energy (G_c) equals the total area of the triangle, as depicted in Figure 2. Consequently, when the energy state exceeds its threshold, delamination progresses.

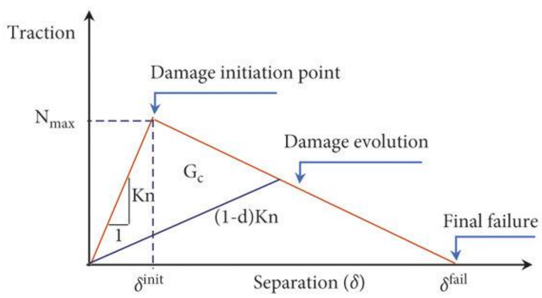

Figure 2 Traction–separation behavior.

In multimode scenarios, the Benzeggagh–Kenane (B–K) fracture criterion, as outlined in Benzeggagh et al. (1996), is used to regulate the delamination progression. The following formula was delineated by SIMULA (2020) :

$$G_n^c + (G_s^c - G_n^c)\left(\frac{G_S}{G_T}\right)^{\eta} \leq G^c \tag{11}$$

where the material parameters are $G_T = G_n + G_S$, $\eta = 1.45$, and $G_S = G_s + G_t$.

DOI: 10.5614/j.eng.technol.sci.2026.58.4.10

Results

Energy Partitioning and Damage Initiation Threshold

Figure 3 presents the numerical energy history during the 8.25 J impact event. The artificial energy generated by the hourglass modes peaked at 0.073 J, representing less than 1% of the total internal energy, which is well below the 5% reliability threshold recommended by Dassault Systèmes (2024). Damage apparently initiated at ~0.84 ms, corresponding to a threshold force of 2300 N. Beyond this point, the internal energy associated with damage dissipation steadily increased until stabilizing at 2.0 J at 2.48 ms, coinciding with the minimum kinetic energy (6.1 J) and marking the transition to a steady-state damage condition.

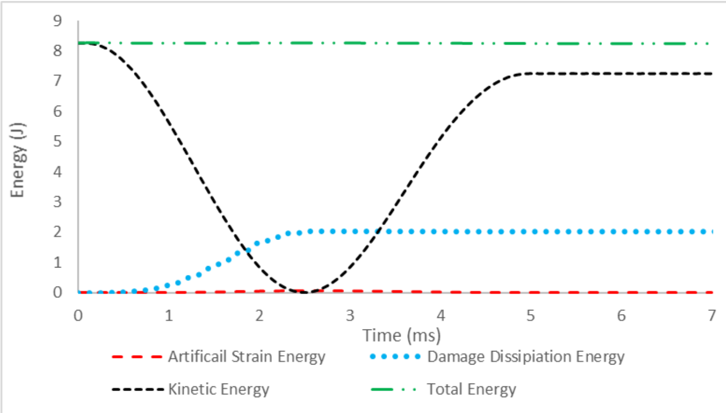

Figure 3 Numerical analysis - energy history.

Force–Time and Force–Displacement Histories

Figure 4 compares the experimental and numerical force–time responses. The mean experimental peak force across the five specimens was 4360 N, whereas the FEM prediction reached 4950 N, indicating a 13% overestimation. The time-to-peak-force occurred at 2.63 ms experimentally and 2.48 ms in the simulation. The experimental scatter exhibited a coefficient of variation (CoV) of 5–10% for the peak force, which is consistent with the typical variability in woven composite impact testing.

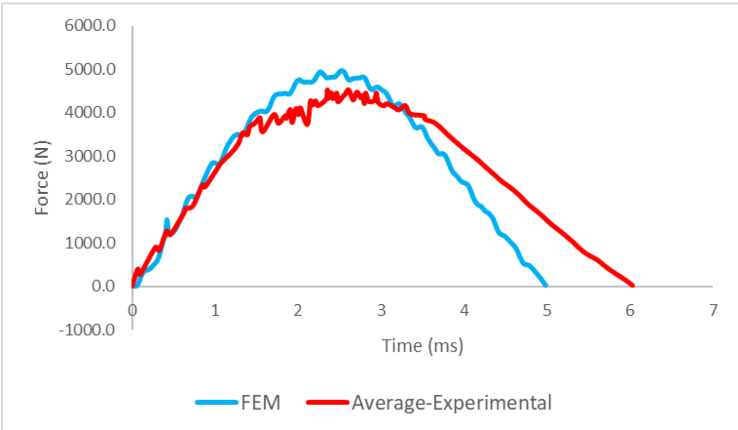

Figure 4 Force–time history recorded during the impact event. Solid red line: mean of five experimental specimens (CoV for peak force in composite impact testing: 5–10%); solid blue line: FEM results.

Figure 5 presents the force–displacement curves. The mean experimental absorbed energy was 3.15 J, whereas the FEM simulation predicted 1.95 J, representing a 40% underestimation. The numerical curve also displayed a steeper initial slope, indicating that the SC8R continuum shell elements slightly overestimated the bending stiffness of the laminate before the onset of damage.

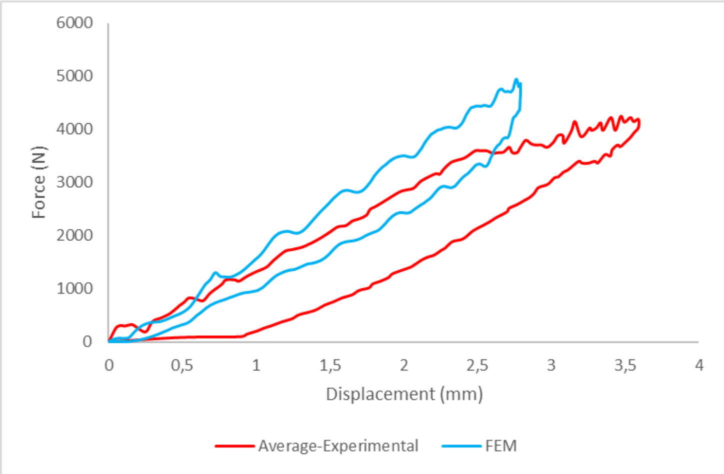

Figure 5 Force–displacement curves: Solid red line: mean experimental results (CoV for absorbed energy: 5–10%); solid blue line: FEM.

Delamination Morphology and Interlaminar Profiles

The ultrasonic C-scan projections (Figure 6) reveal that delamination diameters across the five specimens ranged from 15.9 to 19.9 mm, with an average of 17.9 mm. The experimental damage boundaries exhibited irregular, jagged edges with multidirectional crack branching.

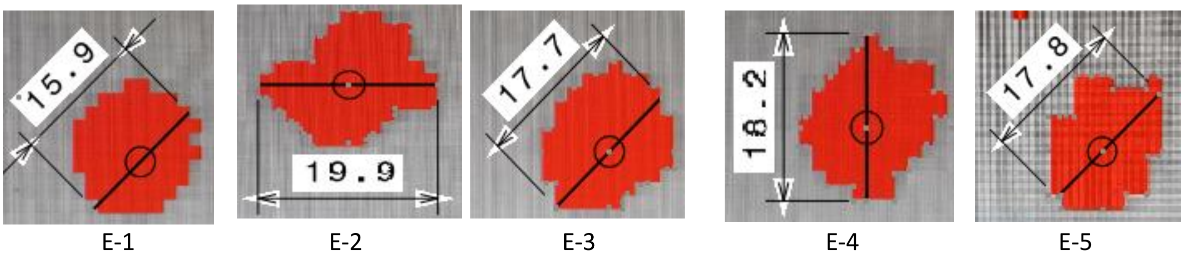

Figure 6 Experimental results for the projection of delamination profiles (E-1–E-5).

The layer-by-layer FEM delamination profiles (Figure 7) showed distinct morphological variations across the seven interlaminar interfaces. The outermost interfaces adjacent to |±45°| plies displayed a star-like propagation pattern, while mid-thickness interfaces adjacent to |0°/90°| plies exhibited more elliptical, symmetric shapes. The numerical delamination boundaries were consistently smooth and lacked the experimentally observed edge irregularities. Figure 8 overlays the projected delamination extents from both approaches, confirming that the FEM successfully captured the overall damage footprint and maximum diameter, despite the absence of localized edge roughness.

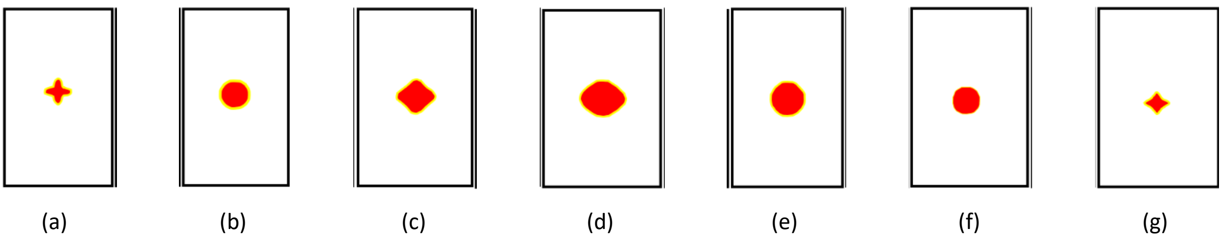

Figure 7 Delamination in the interlaminar layer (left to right, 1st to 7th layer): FEM results. (a) (|±45°|/|90°/0°|), (b) (|90°/0°|/|±45°|), (c) (|±45°|/|90°/00), (d) (|90°/0°|/|0°/90°|), (e) (|90°/0°|/|±45°|), (f) (|±45°|/|90°/0°|), (g) (|90°/0°|/|±45°|).

DOI: 10.5614/j.eng.technol.sci.2026.58.4.10

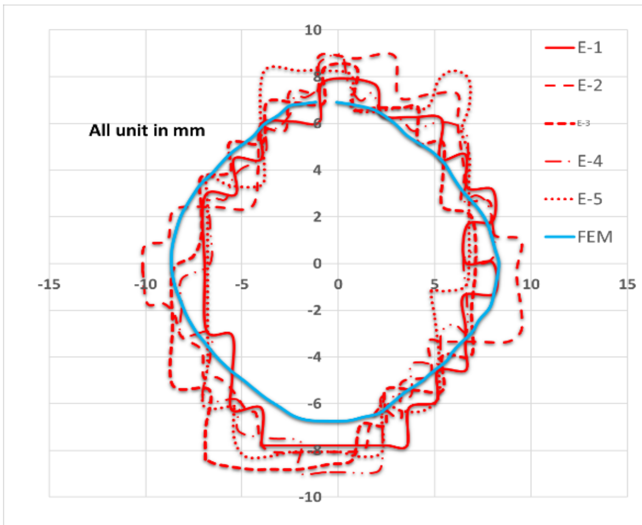

Figure 8 Projected Delamination. Experiments (E-1 to E-5) vs. FEM.

Discussion

Interpretation of Dynamic Response and Energy Dissipation Discrepancies

The 13% overestimation of the peak force and the 40% underestimation of the absorbed energy highlight fundamental differences in how impact energy dissipated in the numerical model and physical specimen. The earlier attainment of the peak force in the FEM compared with that in experiments (2.48 vs. 2.63 ms, respectively) was primarily attributed to the lumped-mass formulation and the absence of distributed inertial effects, which delay stress-wave propagation in real laminates. Additionally, the SC8R continuum shell elements inherently overpredicted the initial bending stiffness as they did not account for the microscale resin-rich zones or ply waviness that reduced the effective flexural rigidity in woven architectures.

The significant gap in the experimental and numerically predicted absorbed energy (3.15 vs. 1.95 J, respectively) confirmed that the homogeneous cohesive zone model (CZM) captured only matrix-dominated interlaminar fracture, while omitting critical intralaminar and interface energy sinks. In the physical specimens, energy was additionally dissipated through fiber bridging, transverse matrix microcracking, interlaminar friction, and localized fiber breakage at the yarn crossover points. These mechanisms collectively increased the effective fracture toughness and delayed crack arrest, explaining why the experimental force–displacement curve maintained higher load levels over longer displacements. The damage initiation threshold at 0.84 ms (2300 N) aligned with the critical load required to overcome interlaminar shear strength at ±45°/0° interfaces, the point at which delamination transitioned from stable initiation to rapid propagation (Ao et al., 2022).

Interlaminar Failure Mechanisms and Ply Architecture Effects

The morphological contrast between the experimental and simulated delamination directly reflected the influence of the stacking sequence and woven architecture on the interlaminar stress states. The star-like patterns at |±45°| interfaces arose from severe mismatches in the stiffness coefficients and Poisson's ratios between adjacent plies, which concentrated interlaminar shear stresses (τxz, τyz) along the fiber/yarn directions. This shear-driven propagation as consistent with the dominant mode II (in-plane shear) and mode III (out-of-plane tearing) fracture mechanisms. Three analytical indicators corroborated the inference: (1) the alignment of crack fronts with ±45° yarn trajectories, (2) elevated FEM-predicted interlaminar shear stresses at these interfaces during peak loading, and (3) the B–K mixed-mode criterion (η = 1.45), which explicitly couples shear and normal fracture energies to drive crack growth proportional to the local shear stress state (Benzeggagh & Kenane, 1996; SIMULA, 2020).

Conversely, the more symmetric, elliptical delamination at the mid-thickness |0°/90°| interfaces reflected a larger contribution from Mode I (opening) stress driven by bending-induced through-thickness tension and stress-wave reflection at the laminate core. The jagged, irregular edges observed experimentally but absent in the FEM resulted from localized fiber bridging and matrix fragmentation in the resin-rich interyarn regions. In woven composites, intact fibers spanning delaminated zones resist crack opening, effectively increasing the apparent fracture energy (Gc) and forcing cracks to deviate along tortuous paths (Liu et al., 2020; Andrew et al., 2019). These findings aligned with those of Ma et al. (2024), who demonstrated that woven laminates exhibited greater delamination complexity than UD systems owing to ply-interaction effects and fiber undulation.

Model Limitations, Validation Scope, and Research Flow Implications

Although the current CZM framework successfully predicted the global delamination footprint and peak load timing within acceptable engineering tolerances, it assumed a homogeneous interface, thereby systematically smoothing out local stress perturbations induced by woven yarn waviness. This limitation explains why the simulation underestimated the energy dissipation and failed to reproduce edge irregularities; however, it remained sufficient for preliminary damage-tolerance screening.

From a research flow perspective, these results established a clear validation boundary: the proposed FEM methodology was highly effective in predicting the extent of delamination, force–time response, and interlaminar failure initiation in aerospace-representative woven laminates. However, to accurately quantify the absorbed energy and residual strength degradation, next-generation models must integrate mesoscale fabric geometry, traction–separation laws with plateau regions (to simulate fiber bridging), and distributed-mass formulations. By explicitly linking the ~40% energy discrepancy and morphological differences to unmodeled physical mechanisms, this study provides a structured pathway for advancing damage prediction in woven composites. The validated framework can be directly applied to multi-energy impact studies and CAI assessments, whereas the identified limitations provide targeted improvements in cohesive modeling for hybrid and repaired composite architectures.

Conclusions

This study comprehensively evaluated the low-velocity impact damage tolerance of woven AS4/8552 carbon/epoxy laminates through a combined experimental and FEM approach. By integrating continuum shell elements with a cohesive zone model governed by the Hashin failure criterion and B–K mixed-mode law, the numerical framework successfully captured the dynamic impact response, peak force magnitudes, and overall delamination morphology observed in 8.25 J drop-weight tests. The FEM-predicted peak force deviated from the experimental results by only 13%, and the simulated delamination footprint closely matched the ultrasonic C-scan measurements, confirming the robustness of the model for preliminarily screening for damage tolerance in aerospace-grade woven architectures. However, systematic discrepancies were identified: the simulation underestimated the absorbed energy by ~40% and produced delamination boundaries that were smoother than the jagged experimental edges. These deviations stemmed primarily from the inherent limitations of homogeneous cohesive elements and continuum shell formulations, which cannot fully capture energy-dissipating mechanisms such as fiber bridging, intralaminar microcracking, and local stress perturbations induced by woven yarn undulations. Additionally, the use of a lumped-mass formulation introduced minor timing shifts in the force–time history relative to the experimental data.

Despite these limitations, the explicit correlation between the numerical discrepancies and unmodeled physical mechanisms establishes a clear validation boundary and provides a practical baseline for predicting BVID in secondary aerospace structures. To advance this framework, future research should prioritize several interconnected directions. First, the numerical fidelity can be enhanced by transitioning to distributed mass formulations to correct dynamic timing discrepancies and by implementing advanced traction–separation laws with plateau regions to explicitly simulate fiber bridging and crack-arrest behaviors. Second, experimental and numerical campaigns should be expanded across multiple impact energy levels (e.g., 5–15 J) to develop energy-dependent damage prediction models coupled with CAI testing to directly quantify the degradation of residual strength. Third, intra-laminar damage evolution requires high-resolution characterization using techniques such as micro-CT scanning to resolve the matrix cracking pathways and fiber breakage mechanisms that influence local stress concentrations. Finally, extending this validated cohesive-zone method to hybrid composite systems (e.g., CFRP–GFRP) and structurally repaired configurations (e.g., stepped or scarf joints) will significantly broaden its industrial applicability and support next-generation protocols for certifying damage tolerance.

Acknowledgment

The Institute of Technology, Bandung, fully funded the present work through the P2MI 2024 fiscal year. The Indonesian Aircraft Industry supports the testing facilities, material data, and test specimen preparation.

DOI: 10.5614/j.eng.technol.sci.2026.58.4.10

Compliance with ethics guidelines

The authors declare they have no conflict of interest or financial conflicts to disclose.

This article contains no studies with human or animal subjects performed by the authors.

References

Andrew, J. J., Srinivasan, S. M., Arockiarajan, A., & Dhakal, H. N. (2019). Parameters influencing the impact response of fiber-reinforced polymer matrix composite materials: A critical review. Composite Structures, *224*, 111007. https://doi.org/10.1016/j.compstruct.2019.111007

Anuse, V. S., Shankar, K., Velmurugan, R., & Ha, S. K. (2022). Compression-After-Impact analysis of carbon fiber reinforced composite laminate with different ply orientation sequences. International Journal of Impact Engineering, *167*, 104277. DOI: 10.1016/j.ijimpeng.2022.104277.

Ao, W., Zhuang, W., Xing, B., Zhou, Q., & Xia, Y. (2022). Finite element method of a progressive intralaminar and interlaminar damage model for woven fibre laminated composites under low velocity impact. *Materials & Design*, *223*, 111256. https://doi.org/10.1016/j.matdes.2022.111256

ASTM D7136/D7136M-25. (2025). Standard Test Method for Measuring the Damage Resistance of a Fiber-Reinforced Polymer Matrix Composite to a Drop Weight Impact Event.

Benzeggagh, M. L., & Kenane, M. (1996). Measurement of mixed-mode delamination fracture toughness of unidirectional glass/epoxy composites with mixed-mode bending apparatus. *Composites Science and Technology*, *56*(4), 439–449. https://doi.org/10.1016/0266-3538(96)00005-x

Dassault Systems Simulia Corp. (2024). Abaqus 2024 Documentation. https://help.3ds.com

Fanteria, D., Lazzeri, L., Panettieri, E., Mariani, U., & Rigamonti, M. (2017). Experimental characterization of the interlaminar fracture toughness of a woven and a unidirectional carbon/epoxy composite. *Composites Science and Technology*, *142*, 20–29. https://doi.org/10.1016/j.compscitech.2017.01.028

Fawcett, A. J., & Oakes, G. D. (2006). Boeing Composite Airframe Damage Tolerance and Service Experience. Proceedings of the FAA Composite Damage Tolerance and Maintenance Workshop, Chicago, IL, 19–21 July 2006. Boeing Commercial Airplanes.

Grasso, M., Xu, Y., Ramji, A., Zhou, G., Chrysanthou, A., Haritos, G., & Chen, Y. (2019). Low-velocity impact behaviour of woven laminate plates with fire retardant resin. *Composites Part B: Engineering*, *171*, 1–8. https://doi.org/10.1016/j.compositesb.2019.04.023

Hashin, Z. (1980). Failure criteria for unidirectional fiber composites. *Journal of Applied Mechanics*, *47*(2), 329–334. https://doi.org/10.1115/1.3153664

Hexcel Corporation (2020). AS4/8552 Epoxy Matrix, Intermediate Modulus Fiber – Material Properties. *Product Data Sheet*. https://www.hexcel.com/Resources/DataSheets/Prepreg-Materials/AS4-8552

Sanga, R. P. L., Garnier, C., & Pantalé, O. (2016). Finite element simulation of low velocity impact damage on an aeronautical carbon composite structure. *Applied Composite Materials*, *23*(6), 1195–1208. https://doi.org/10.1007/s10443-016-9508-1

Liu, B., Xu, F., Qin, J., & Lu, Z. (2017). Study on impact damage mechanisms and TAI capacity for the composite scarf repair of the primary load-bearing level. *Composite Structures*, *181*, 183–193. https://doi.org/10.1016/j.compstruct.2017.08.087

Liu, B., Han, Q., Zhong, X., & Lu, Z. (2019). The impact damage and residual load capacity of composite stepped bonding repairs and joints. *Composites Part B: Engineering*, *158*, 339–351. https://doi.org/10.1016/j.compositesb.2018.09.096

Liu, B., Li, F., Liu, Y., & Zhang, Y. (2024). Experimental and numerical studies on low-velocity impact of laminated C/SiC structures. *Composite Structures*, *329*, 117765. https://doi.org/10.1016/j.compstruct.2023.117765

Liu, L., Li, F., Zhao, Z., Zhang, X & Liu, B. (2026). Impact damage and compression after impact on the CFRP-GFRP hybrid composite materials applied to aero-smart-skins. *Proceedings of the Institution of Mechanical Engineers, Part L: Journal of Materials: Design and Applications*. https://doi.org/10.1177/14644207261418448.

Ma, B., Cao, X., Feng, Y., Song, Y., Yang, F., Li, Y., Zhang, D., Wang, Y., & He, Y. (2024). A comparative study on the low velocity impact behavior of UD, woven, and hybrid UD/woven FRP composite laminates. *Composites Part B: Engineering*, *271*, 111133. https://doi.org/10.1016/j.compositesb.2023.111133

SIMULA (2020). Defining the Constitutive Response of Cohesive Element Using Traction-Separation Description

Suada, M. G., Syamsudin, H., & Simanjorang, H. C. (2019). Finite element analysis of composite plate subject to low-velocity impact and compression after impact. Proceedings of the 10th AUN/SEED-Net Regional Conference on Mechanical and Manufacturing Engineering (RC MEManuE 2019), 7–8 November 2019, Phnom Penh, Cambodia.

Suada, M. G., Syamsudin, H. & Romadon, H. (2022). Experimental and numerical analysis of carbon/epoxy composite plate subject to low-velocity impact. *Journal of Engineering and Technological Sciences*, *54*(2), 220204. https://doi.org/10.5614/j.eng.technol.sci.2022.54.2.4

Tosti Balducci, G., & Chen, B. (2024). Overcoming the cohesive zone limit in the modelling of composites delamination with TUBA cohesive elements. *Composites Part A: Applied Science and Manufacturing*, *185*, 108356. https://doi.org/10.1016/j.compositesa.2024.108356

Manuscript Received: 29 September 2025
1st Manuscript Revision Received: 17 March 2026
2nd Manuscript Revision Received: 30 April 2026
Accepted Manuscript: 10 June 2026